Chemical Engineering Science 320 (2026) 122485

Contents lists available at ScienceDirect

Chemical Engineering Science

journal homepage: www.elsevier.com/locate/ces

Electron density engineering in Pd/H-TiO_2 catalysts for enhanced photocatalytic CO_2 to formic acid☆

Ruijie Ma [a,b], Huimin Gao [a,b], Jinpeng Zhang [a,b], Jieying Jing [a,b,*], Wen-Ying Li [a,*]

[a] State Key Laboratory of Clean and Efficient Coal Utilization, Taiyuan University of Technology, Taiyuan 030024, China
[b] College of Chemical Engineering and Technology, Taiyuan University of Technology, Taiyuan 030024, China

ARTICLE INFO

Keywords:
Photocatalytic CO_2 reduction
Formic acid production
Pd/H-TiO_2 catalysts
Electron-hole separation
Hydrogenated TiO_2

ABSTRACT

Photocatalytic reduction of CO_2 to formic acid (HCOOH) offers a sustainable pathway for carbon utilization, yet its efficiency is fundamentally limited by poor CO_2 adsorption and rapid electron-hole recombination in conventional photocatalysts. To address this challenge, a series of Pd-loaded hydrogenated TiO_2 catalysts (x wt%Pd/H-TiO_2) were developed through a synergistic hydrogen reduction-impregnation strategy, aiming to regulate the electron density of Pd active sites and enhance interfacial charge separation. Systematic characterization revealed that increasing Pd loading (0.6–1.4 wt%) effectively trapped photogenerated electrons, suppressing recombination losses and elevating electron density at Pd sites. Combined with optimized CO_2 adsorption capacity (0.178 mmol·g^{-1}) and accelerated charge transfer, the 1.0 wt%Pd/H-TiO_2 catalyst achieved a HCOOH production rate of 14.14 mmol·g_{cat}^{-1}·h^{-1} under mild conditions (30 °C, 2.0 MPa, 4.57 mW·cm^{-2}), outperforming most reported TiO_2-based systems. Mechanistic studies further demonstrated a strong correlation between Pd-induced electronic effects and multi-electron CO_2 activation kinetics. This work provides a scalable catalyst design paradigm for balancing charge dynamics and surface reactivity in photocatalytic CO_2 valorization.

1. Introduction

The chemical transformation of the greenhouse gas carbon dioxide (CO_2) plays a crucial role in addressing environmental challenges. As an effective element with high abundance of both C and O, CO_2 can be transformed into valuable compounds such as carbon monoxide (CO), methanol (CH_3OH), methane (CH_4), formic acid (HCOOH), ethylene (C_2H_4) and others, opening up new paths for CO_2 capture and exploitation (Wang et al., 2023; Xu et al., 2023). Among the reduction products, HCOOH has gained interest because it is a raw material for several chemical processes (Rumayor et al., 2018). It can also serve as a hydrogen-storage molecule that contains 4.4 wt% hydrogen (Bi et al., 2016; Zhao et al., 2023). HCOOH from CO_2 hydrogenation has been comprehensively investigated. Owing to the high thermodynamic stability of CO_2 molecule, with bond energies reaching 750 kJ·mol^{-1}, considerable energy is necessary for the cleavage of C=O bonds (Wagner et al., 2020). The process of hydrogenating CO_2 to prepare HCOOH by photocatalysis technology can utilize renewable energy sources to activate inert CO_2 molecules. Compared with other typical methods of CO_2 conversion, photocatalytic hydrogenation of CO_2 to prepare HCOOH not only has 100 % atom utilization, but also enables the reaction to be conducted under mild conditions instead of the traditional high temperature and high-pressure conditions (Wang et al., 2021).

However, the photocatalytic CO_2 reduction reaction also has unavoidable disadvantages (Ma et al., 2024). Firstly, weak interaction between conventional photocatalyst surface and CO_2 molecules makes less CO_2 adsorption (Alamgir et al., 2025). The linear structure and closed-shell electronic configuration of the CO_2 molecule shows a more stable nature making it difficult to be activated (Habisreutinger et al., 2013). Secondly, the CO_2 photocatalytic reduction process involves a multi-electron transfer mechanism that requires the coupling of multiple electrons and protons to facilitate the chemical transformation (Pan and Heagy, 2020; Zhang et al., 2023). Unfortunately, photocatalysts have fast electron-hole recombination and the low surface charge density makes it difficult to ensure multiple electron supply (He et al., 2025). Therefore, the adsorption and activation of CO_2 molecule and photocatalytic CO_2 conversion are highly challenging. Jia et al. (Xiong et al., 2023) investigated the activation and dissociation of CO_2 on rutile and anatase titanium dioxide (TiO_2) surfaces, and demonstrated by density functional theory (DFT) calculations that the metal loading effectively

☆ This article is part of a special issue entitled: '100th Anniversary of SCET, TJU' published in Chemical Engineering Science.

* Corresponding authors at: State Key Laboratory of Clean and Efficient Coal Utilization, Taiyuan University of Technology, Taiyuan 030024, China.
E-mail addresses: jingjieying@tyut.edu.cn (J. Jing), ying@tyut.edu.cn (W.-Y. Li).

https://doi.org/10.1016/j.ces.2025.122485
Received 5 June 2025; Received in revised form 18 August 2025; Accepted 20 August 2025
Available online 23 August 2025

promotes the electron transfer and contributes more to the activation of CO_2.

The strategic design of electron-rich active sites is fundamental to enhancing the CO_2 adsorption and activation process (Cao et al., 2024). The introduction of metals has been demonstrated to regulate the electron density of active sites, thereby promoting CO_2 adsorption and activation. Additionally, it can cause electron-hole pairs to separate, which improves CO_2 conversion (Xiong et al., 2015). This is due to injection of electrons into a CO_2 molecule from active sites of catalyst surface can cause bending of the linear structure, thereby activating the CO_2. Zheng et al. (Xiong et al., 2015) prepared photocatalysts using TiO_2 as a carrier loaded with the metal Pt by a simple sol–gel method, and found that two platinum states (Pt^0 and Pt^{2+}) existed in TiO_2. In contrast to the Pt^{2+} species, the Pt^0 species functions as an electron acceptor, thereby effectively attracting photo-induced electrons and markedly improving the adsorption of CO_2 molecules. This observation emphasizes the vital role of electron transport in facilitating the photocatalytic reduction of CO_2 to HCOOH by transferring electrons from the photocatalyst to the active sites. The enhancement of photocatalytic efficiency can be achieved through the improvement of CO_2 adsorption and activation at active sites characterized by elevated electron density (Cao et al., 2021). Ma et al. (Ma et al., 2023) created an oxygen-coordinated Pr single-atom (Pr_1-N_4O_2) catalyst that was 28.9 times more active than it was before to the modification, with an activity of 511 $\mu mol \cdot g^{-1} \cdot h^{-1}$ for the photocatalytic reduction of CO_2 to CH_3OH. The study revealed that the Pr_1-N_4O_2 catalyst more effectively promotes the generation of photogenerated electrons at the Pr sites, than the catalyst lacking oxygen-coordination Pr atoms (Pr_1-N_6), providing high-density active sites that enhance CO_2 adsorption and activation.

Due to its suitable redox potential, TiO_2 has become the most popular material, exhibiting excellent photocatalytic properties. Pd-loaded H-TiO_2 photocatalysts were prepared using hydrogen heat treatment combined with impregnation method. This study aims to explore the influence of electron density at Pd active sites on the adsorption and activation of CO_2, as well as the properties related to electron-hole separation. A variety of catalysts were synthesized by adjusting the loading levels of Pd. The electron density of Pd active sites was modulated via different Pd loading amounts. The results showed that, for the best photocatalytic activity, there was an ideal balance between the Pd active center's electron density, CO_2 adsorption, and electron-hole separation capability. The influence of the variation of Pd contents on CO_2 adsorption activation was further confirmed by density functional theory calculations.

2. Experimental

2.1. Materials

Anatase titanium dioxide (TiO_2; 99.8 %), palladium chloride ($PdCl_2$; 99.9 %), sodium borohydride ($NaBH_4$; 98 %), potassium carbonate (K_2CO_3; 98 %), potassium hydroxide (KOH; 95 %), and a standard formic acid solution (HCOOH; AR) were bought from Aladdin Reagent (Shanghai) Co.,Ltd.

2.2. Synthesis of catalyst

Anatase TiO_2 was acquired commercially and used as the precursor material without further purification (hereafter denoted as TiO_2). To prepare hydrogenated TiO_2 (designated as H-TiO_2), the pristine TiO_2 was subjected to a pretreatment process. The procedure entailed subjecting the material to a temperature of 500 °C for a duration of 12 h within a reducing atmosphere composed of 5 % hydrogen (H_2) complemented by argon (Ar).

The x wt% Pd/H-TiO_2 catalysts were synthesized employing a traditional impregnation technique (Jin et al., 2020). In a typical synthesis procedure, predetermined amounts of $PdCl_2$—with its concentration adjusted to achieve the desired metal loading—were combined with 0.5 g of H-TiO_2 support and 20 mL of deionized water. The mixture was prepared in a glass beaker under controlled conditions. The mixture underwent continuous stirring at room temperature for a duration of 24 h to guarantee thorough dispersion, culminating in a homogeneous suspension. Subsequently, the pH of the suspension was meticulously adjusted to a range of 10.0–11.0 utilizing a 1 $mol \cdot L^{-1}$ NaOH aqueous solution. The molar ratio of Pd to $NaBH_4$ was maintained at 1:6 by adding a freshly prepared aqueous solution of $NaBH_4$ (30 $mg \cdot mL^{-1}$) to the alkaline suspension. The reduction reaction was permitted to proceed for 2 h with continuous stirring, and the process considered complete when gas evolution ceased. Vacuum filtration was employed to isolate the solid product, which was then extensively washed with deionized water to eliminate any soluble residues. The final catalyst, known as Pd/H-TiO_2, was obtained by drying the material in an oven at 110 °C for 12 h after purification.

2.3. Catalyst characterization

The structural characteristics of TiO_2, H-TiO_2, and x wt% Pd/H-TiO_2 catalysts were analyzed using X-ray diffraction (XRD; Rigaku Ultima IV) to assess their crystallinity and phase composition. The quantitative analysis of palladium loading in x wt% Pd/H-TiO_2 was performed utilizing inductively coupled plasma-optical emission spectrometry (ICP-OES; Agilent 5110). The morphological characterization, which encompassed the size distribution of Pd nanoparticles, was conducted utilizing transmission electron microscopy (TEM) and high-resolution transmission electron microscopy (HRTEM; JEOL JEM-2100F). The investigation of surface electronic states was conducted using X-ray photoelectron spectroscopy (XPS; Thermo Scientific K-Alpha). Photoelectrochemical properties were evaluated using a CHI 760E electrochemical workstation, while charge carrier separation efficiency was assessed through photoluminescence (PL) spectroscopy. Adsorption characteristics were quantified by CO_2 temperature-programmed desorption (CO_2-TPD; Micromeritics AutoChem II 2920) to measure CO_2 uptake capacity.

2.4. CO_2 hydrogenation performance

The experiments for photocatalytic CO_2 reduction were carried out in a 50 mL high-pressure autoclave reactor equipped with a sapphire optical window (Anhui Kemi Machinery Technology Co., Ltd.). The reaction system was sustained at a temperature of 30 ± 0.5 °C, under a total pressure of 2.0 MPa. The reactor was charged with an aqueous mixture containing 10 mL deionized water, 10 mL KOH solution, and catalyst at a concentration of 2 $g \cdot L^{-1}$. Prior to the initiation of the reaction, the reactor underwent a tri-fold purging process utilizing high-purity CO_2 (99.99 %) to ensure the complete removal of any ambient gases. The reaction atmosphere was established by introducing 1.0 MPa of CO_2, followed by 1.0 MPa of H_2 through separate gas inlets. Photocatalytic activation was achieved using a monochromatic ultraviolet (UV) light source ($\lambda = 300$ nm) directed vertically through the sapphire window. Precise temperature control (±0.1 °C) was maintained throughout the experiment using a calibrated thermocouple integrated with the reactor jacket. Gas products were analyzed by gas chromatography (GC, Agilent 8890). Liquid products were analyzed by high performance liquid chromatography (HPLC, Agilent 1260 Infinity II). The HCOOH production rate was determined according to equation (1).

$$Y = \frac{n_{HCOOH}}{m_{cat.} \times t} \quad (1)$$

where n_{HCOOH} denotes the amount of HCOOH after the reaction (mmol), $m_{cat.}$ is the mass of catalyst (g), and t is the reaction time (h).

2.5. Theoretical calculations

The influence of metal Pd enrichment and oxygen vacancies (O_v) on CO_2 adsorption and activation mechanisms was examined through DFT.

Structural representations of the TiO_2 (101) facet were constructed utilizing data acquired from high-resolution transmission electron microscopy (HRTEM) analysis. The Vienna Ab initio Simulation Package (VASP) was employed to carry out quantum mechanical simulations, utilizing the projector augmented wave (PAW) method for electronic structure calculations (Zheng et al., 2021; Li et al., 2018). The PAW method was utilized to examine the interaction between the core and valence electrons. The valence electron states were expanded utilizing a plane wave basis set, employing a cutoff energy of 400 eV for the purpose of total energy calculations. The self-consistent electronic loop was deemed converged upon achieving a convergence criterion of 10^{-5} eV. The convergence of the calculation is established when the maximal force exerted on an atom falls below 0.02 eV $Å^{-1}$. The TiO_2 (101) surface was characterized by a vacuum layer thickness of 15 Å and a 2 × 2 × 1 Monkhorst-Pack k-point mesh. The adsorption energy (E_{ads}) of CO_2 on the catalyst is calculated utilizing equation (2):

$$E_{ads} = E_{total} - E_{catalyst} - E_{CO_2} \quad (2)$$

where E_{total} represents the total energy of CO_2 molecule adsorbed on Pd metal particles supported on H-TiO_2.$E_{catalsyt}$ denotes the total energy of the Pd/H-TiO_2 system, and E_{CO_2} is the total energy of gas molecules. The charge density difference (Δρ) was computed according to equation (3).

$$\Delta\rho_{AB} = \rho_A - \rho_B \quad (3)$$

where $\Delta\rho_{AB}$, ρ_A, and ρ_B is charge densities of the systems AB (CO_2 adsorbed on Pd_x/TiO_2-O_v or Pd_x/TiO_2), A (CO_2 or CO_2 − Pd of CO_2 adsorbed on Pd_x/TiO_2), B (Pd_x/H-TiO_2 or TiO_2-O_v of CO_2 adsorbed on Pd_x/TiO_2-O_v), respectively. The interactions and charge transfer between Pd and TiO_2 were examined separately since it is crucial to note that their roles in the system are still unclear.

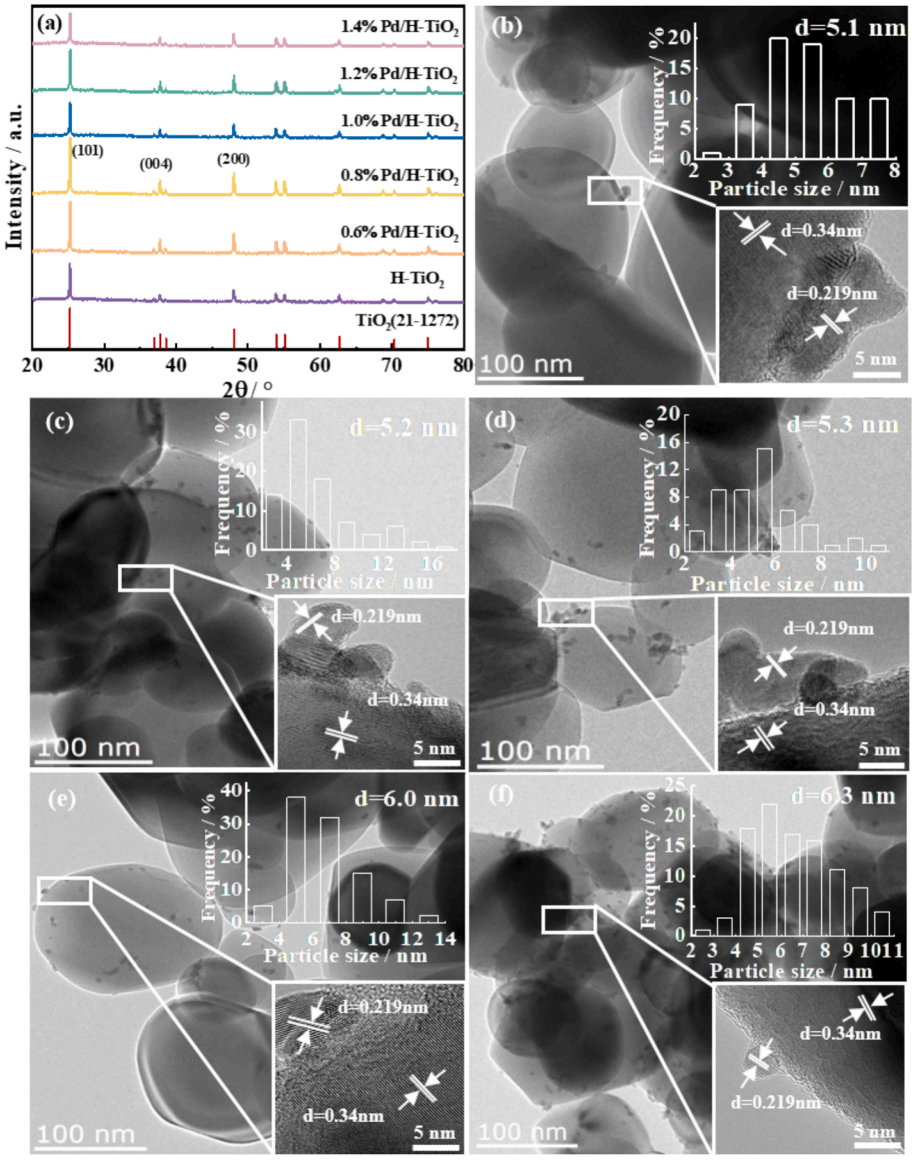

Fig. 1. (a) XRD pattern of x wt%Pd/H-TiO_2 catalysts, and HRTEM images of (b) 0.6 %Pd/H-TiO_2 catalyst, (c) 0.8 %Pd/H-TiO_2 catalyst, (d) 1.0 %Pd/H-TiO_2 catalyst, (e) 1.2 %Pd/H-TiO_2 catalyst, (f) 1.4 %Pd/H-TiO_2 catalyst. The inserts are Pd particle size distribution and enlarged HRTEM images.

3. Results and discussion

3.1. Microstructure

The crystalline structure of the x wt%Pd/H-TiO_2 catalysts were analyzed using XRD, as shown in Fig. 1a. The x wt%Pd/H-TiO_2 catalysts all contained three major diffraction peaks at around 25.3°, 37.9° and 48.1° were assigned to (101), (004), and (200) (JCPDS No. 21–1272). With the increase of Pd loading, its diffraction peaks did not appear in the catalysts, indicating that Pd atoms size is small (Permporn et al., 2022). The main characteristic peaks are not significantly shifted, which proves that Pd has not entered the lattice of H-TiO_2 but is highly dispersed across the surface of H-TiO_2 catalysts. In order to investigate the influence of metal Pd loading on the grain size of H-TiO_2, the Scherrer equation was utilized to determine the crystallite size for all samples, as presented in Table S1. The results showed that all samples are between 38 and 40 nm. By measuring the Pd content in the catalysts, it was found that the theoretical content was consistent with the actual content, showing that x wt%Pd/H-TiO_2 catalysts could be successfully prepared by the impregnation method.

Through the analysis of lattice stripe spacing in the HRTEM maps of various x wt% Pd/H-TiO_2 catalysts, it was determined that a consistent stripe spacing of 0.219 nm was present across all catalysts, which is indicative of the Pd (1 1 1) orientation. And all of the samples show a 0.34 nm lattice stripe, which corresponds to H-TiO_2 (1 0 1). It can be found that the loading of Pd has no effect on the microscopic morphology of H-TiO_2, indicating the microstructure of Pd/H-TiO_2 catalysts prepared by impregnation can remain stable. In photocatalytic reactions, the size of metal particles can influence the photocatalytic activity (Wang et al., 2018). The dimensions of the Pd particles were ascertained via TEM, owing to the significant relationship between the chemical processes on the catalyst surface and the movement of photogenerated electrons. As shown in Fig. 1b-f, the size of Pd particles increases progressively with the Pd loading content. When the Pd loading exceeds 1.0 %, a rapid increase in particle size is observed, reaching approximately 6.0 nm. Photocatalytic reactions prefer small metal particle size to enhance electron transfer (Schweinberger et al., 2013).

Introduction of the metal Pd promotes electron transport to the active site and modifies its electron density (Cao et al., 2024). In order to deeply investigate the changes in the electron density at the Pd active center, XPS was used to analyze the electronic structure of Pd and Ti in the catalyst, as shown in Fig. 2. The investigation revealed that an increase in the number of metal active sites results in a redistribution of surface charge density, which subsequently alters the electronic structure of Pd (Zhang et al., 2013). It can be seen that there is one type of Pd state (Pd^0), in x wt% Pd/H-TiO_2 catalysts. compared to the Pd^{2+} species, Pd^0 species may function as an electron acceptor, causing electron segregation and raising the Pd active site's electron density (Jin et al., 2020). As illustrated in Fig. 2a, the binding energy of Pd $3d_{3/2}$ across all catalysts exhibits a shift towards higher binding energy, while the binding energy of Ti $2p_{3/2}$ demonstrates a shift towards lower binding energy. This observation suggests a notable interaction between H-TiO_2 and the metal Pd. The electrons are transferred from the H-TiO_2 to the Pd active sites in all the prepared catalysts. Therefore, the electron density of the Pd active center increases. It is also possible to observe that the change in binding energy gradually decreases when the loading of Pd exceeds 1.0 %, which indicates a change in the interaction between Pd and H-TiO_2. Moreover, there is a progressive reduction in the electron density of the Pd active center. The variation in the binding energy of metal Pd for x wt% Pd/H-TiO_2 catalysts is presented in Table S2.

The textural properties of x wt%Pd/H-TiO_2 catalysts were investigated using N_2 adsorption–desorption measurements. As illustrated in Fig. S1, the catalysts demonstrate a significant specific surface area, which is essential for CO_2 adsorption, as it offers numerous accessible adsorption sites. Significantly, elevated Pd loading led to a marked decrease in surface area (Table S3), suggesting that metallic Pd particles occupy the catalytic surface. The incorporation of metal active sites influences the electron density in the catalyst's active regions, leading to an augmented transfer and localization of induced electrons within these metal active sites, thereby improving the adsorption of CO_2 molecules (Sun and Huang, 2022; Etim et al., 2021; Gao et al., 2023). The influence of electron density at the Pd metal active sites on CO_2 adsorption and activation was assessed by analyzing the interaction between CO_2 molecules and the catalyst using CO_2-TPD locharacterization. As shown in Fig. 3, the series of x wt% Pd/H-TiO_2 catalysts exhibit distinct CO_2 desorption peaks between 200 and 500 °C, demonstrating their pronounced CO_2 chemisorption capability. This behavior originates from the amphoteric nature of the H-TiO_2 support, which possesses both acidic Ti^{4+} sites and basic O^{2-} sites, with the latter

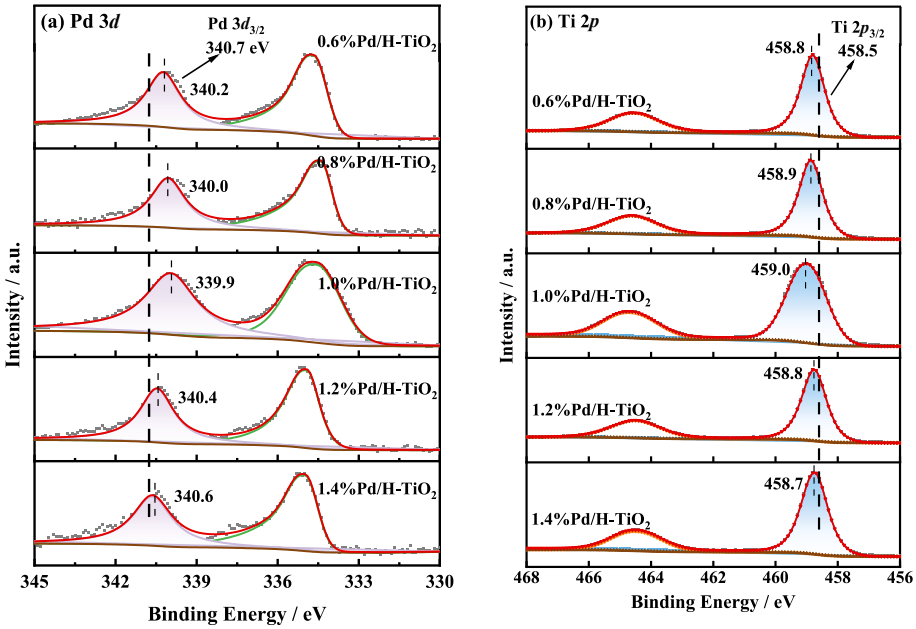

Fig. 2. XPS spectra of (a) Pd 3*d*; (b) Ti 2*p* for x wt%Pd/H-TiO_2 catalysts.

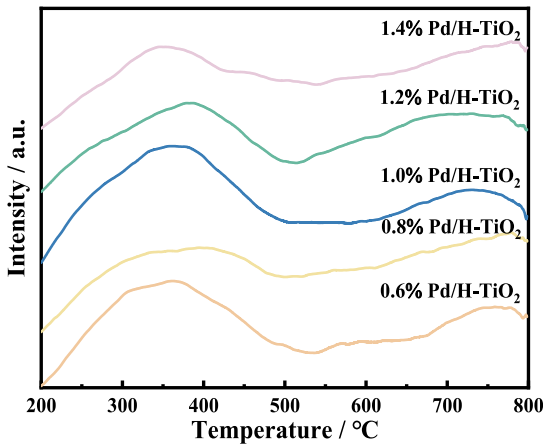

Fig. 3. CO_2-TPD curves of x wt% Pd/H-TiO_2 catalysts.

particularly facilitating CO_2 adsorption through the formation of carbonate-like species. The calculated CO_2 adsorption amounts for x wt % Pd/H-TiO_2 catalysts were summarized in Table S3. As shown in the results, the CO_2 adsorption capacity exhibits a volcano-shaped trend with increasing Pd concentration, initially rising and subsequently decreasing. This behavior clearly demonstrates that the population of metallic active sites plays a pivotal role in governing the CO_2 adsorption dynamics. Notably, the 1.0 wt% Pd/H-TiO_2 catalyst displays the optimal CO_2 adsorption performance, achieving a maximum adsorption capacity of 0.178 mmol·g^{-1}.

3.2. Theoretical calculation

The analysis indicates that the electron density of the metal active sites influences the adsorption performance of the catalyst on CO_2, subsequently impacting the catalyst's activity. Thus, DFT calculations were utilized to evaluate the impact of the number of Pd active sites on CO_2 adsorption and activation. Drawing upon the prior research conducted by the subject group, we developed models incorporating varying Pd contents to investigate the adsorption and activation mechanisms of CO_2, as illustrated in Fig. S2 and Fig. S3. The site of the oxygen vacancy was exemplified by O_{v1}, henceforth referred to as O_v. The adsorption energy and electron transfer of CO_2 in different models are shown in Table 1. CO_2 adsorption on a TiO_2 surface containing O_v can be −0.357 eV, implying that O_v enhances the interaction between CO_2 and the catalyst, hence boosting CO_2 sorption. The analysis of the adsorption energy of CO_2 on catalysts exhibiting varying Pd loadings indicates that at a Pd atom count of 4, the adsorption energy of CO_2 measures −0.236 eV. When the atomic number of Pd was increased to 8, the adsorption energy of CO_2 was even more negative at −0.732 eV, suggesting that the adsorption efficacy of the catalyst for CO_2 could be improved by the addition of Pd atoms. However, the adsorption energy of CO_2 decreased when the number of Pd atoms continued to increase to 12, which was consistent with the experimentally measured HCOOH production rate and CO_2 adsorption. This finding suggests that the production of HCOOH may be optimized by elevating the concentration of the metal Pd within a defined range, as it improves the adsorption of CO_2.

Table 1
Adsorption geometry, energy of CO_2 adsorbed on different Pd loading amounts surface.

Model	TiO_2/(Δe)	Pd_x/(Δe)	CO_2/(Δe)	E_{ads}/eV
CO_2-TiO_2	0.120	–	−0.120	−0.104
CO_2-TiO_2-O_v	0.127	–	−0.127	−0.357
CO_2-Pd_4/TiO_2	−0.325	0.518	−0.193	−0.176
CO_2-Pd_4/TiO_2-O_v	−0.284	0.568	−0.302	−0.236
CO_2-Pd_8/TiO_2	−0.460	0.819	−0.359	−0.337
CO_2-Pd_8/TiO_2-O_v	0.207	0.205	−0.412	−0.732
CO_2-Pd_{12}/TiO_2	−0.567	0.989	−0.422	−0.463
CO_2-Pd_{12}/TiO_2-O_v	−0.003	0.405	−0.402	−0.437

The electron transfer of CO_2 adsorbed on the various catalysts was subsequently analyzed, as illustrated in Fig. 4. When CO_2 is adsorbed on TiO_2-O_v electrons are transferred from TiO_2 to CO_2 (−0.127 e). When further with the increase of Pd loading the charge transfer of CO_2 shows an increasing and then decreasing trend. The charge transfer of CO_2 was at its highest when the number of Pd atoms was 8, suggesting that the activation of CO_2 is improved by the appropriate Pd loading.

3.3. Photocatalytic reduction of CO_2

The photocatalytic performance of x wt%Pd/H-TiO_2 catalysts for the reduction of CO_2 to HCOOH was assessed under controlled conditions: a temperature of 30 °C, a pressure of 2.0 MPa, and a light intensity of 4.57 mW·cm^{-2}. As shown in Fig. 5, the HCOOH production rate initially increases with the Pd loading, reaches a maximum, and subsequently decreases with further increases in metal content. The HCOOH production rate on the H-TiO_2 catalyst is 9.86 mmol·g_{cat}^{-1}·h^{-1}. At an increase in Pd loading amounts from 0.6 % to 1.0 %, the HCOOH production rate increased by about 76 % up to 14.14 mmol·g_{cat}^{-1}·h^{-1}. When the loading of metal Pd continued to increase, the HCOOH production rate decreased instead. Excessive increase in Pd loading is rather detrimental to the catalytic activity. In conjunction with the characterization of Section 3.1, it is possible to observe a progressive increase in the electron density of the Pd active sites as the Pd loading amounts increase, which in turn leads to an improvement in the CO_2 adsorption performance. The increase in CO_2 adsorption is one of the reasons for the improvement of HCOOH production rate. Given that the photocatalytic CO_2 reduction reaction necessitates the migration of electrons to the active sites for the reduction of CO_2, it is essential that only suitable Pd atoms fulfil the function of separating the electron-hole pairs. Thus, the other reason for the lower HCOOH production rate is a higher Pd loading content leads to particle agglomeration and inhibits the effective utilization of metal atoms. The gas products collected after the reaction were analyzed by GC. The results demonstrated that the x wt% Pd/H-TiO_2 catalysts produced virtually no other carbon-containing byproducts, achieving nearly 100 % selectivity for HCOOH. Under identical conditions, the cycling stability of the optimal 1.0 %Pd/H-TiO_2 catalyst was evaluated (Fig. S4). After five consecutive cycles, a slight decrease in HCOOH production rate was observed, which was attributed to a minor reduction in the dispersion of Pd nanoparticles (Fig. S5).

The optical absorption properties of x wt%Pd/H-TiO_2 catalysts were examined using UV–vis diffuse-reflectance spectra (DRS), as shown in Fig. S6. As the Pd loading increases, the catalyst's absorption edge shifts toward the visible range, leading to an enhanced light absorption intensity. This shift can be attributed to the plasmonic resonance effects of Pd nanoparticles, which enhance the absorption of visible light by inducing collective oscillations of conduction electrons in the metal, thus improving the photocatalytic performance under visible light irradiation. According to the Tauc plots (Fig. 6a), the band gap (E_g) of the x wt%Pd/H-TiO_2 catalysts were estimated did not change (2.7 eV) indicating that the metal Pd content does not influence the catalyst's band gap.

The energy band structure of a photocatalyst is critical in determining its redox characteristics, which considerably influence its catalytic activity for CO_2 reduction (Zhang et al., 2021). The catalyst's band structure was evaluated using Mott-Schottky (M−S) characterization to elucidate the causes for the high photocatalytic activity of x wt%Pd/H-TiO_2 catalysts, as shown in Fig. 6b. The n-type semiconductor behavior of the x wt% Pd/H-TiO_2 catalysts was confirmed by the positive slope observed in the M−S curve. The flat band potential, determined by the point at which the tangent to the M−S curve intersects the x-axis, can be used to estimate the conduction band (CB) energy of n-type semiconductors. The application of Formula 4 facilitates the determination of

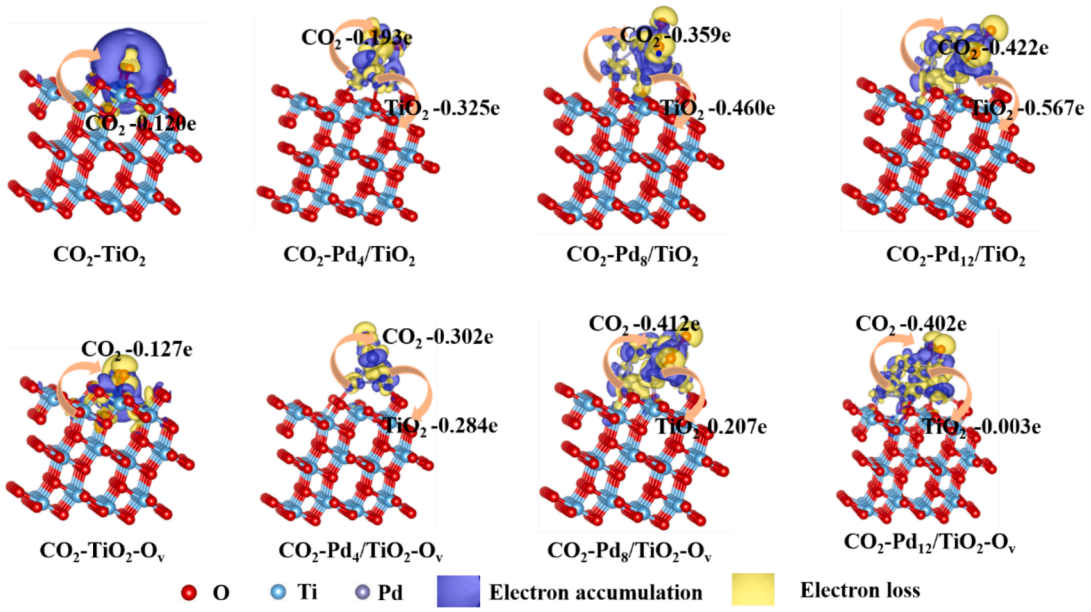

Fig. 4. The charge density difference and Bader charge analysis of models with CO_2 adsorption Pd_x/TiO_2. Yellow and violet denote electron accumulation and loss, respectively (isosurfaces = 0.0006685 e/Bohr^3). Note: This section studies the charge transfer between CO_2 and Pd_x/TiO_2-O_v. (For interpretation of the references to colour in this figure legend, the reader is referred to the web version of this article.)

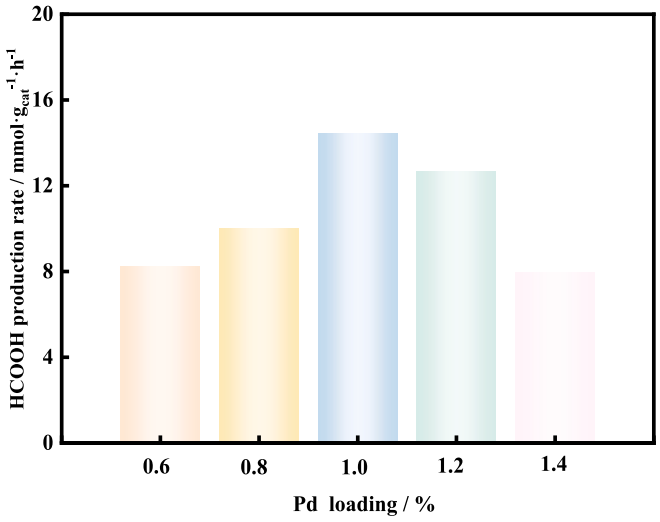

Fig. 5. HCOOH production rate within 1 h of x wt%Pd/H-TiO_2 catalysts;

the potential concerning the Ag/AgCl reference electrode. The valence band (VB) values for Pd/H-TiO_2 concerning the normal hydrogen electrode (NHE) can be determined using Formula 5 (Iguchi et al., 2016):

$$E[vsNHE] = 0.2V + E[vsAg/AgCl] \quad (4)$$

$$E_{VB} = E_g + E_{CB} \quad (5)$$

The flat-band potential of n-type semiconductors has been documented to be 0.1 V more positive than the CB (Huang et al., 2021). Therefore, the calculated ECB values for the x wt% Pd/H-TiO_2 catalysts were −0.71, −0.78, −0.86, −0.67, and −0.62 V versus the NHE, corresponding to different Pd loadings. Detailed energy band structure parameters for the x wt%Pd/H-TiO_2 catalysts are provided in Table S4 and Fig. 7. For the photocatalytic reduction of CO_2 to HCOOH to occur, the catalyst's CB potential must be less than the CO_2/HCOOH potential (−0.58 eV). According to Fig. 7, the result proved that x wt% Pd/H-TiO_2 catalysts met the redox potential for the photocatalytic reduction of CO_2 to HCOOH, indicating that all prepared catalyst can convert CO_2 to HCOOH. Compared with other catalysts, it was also found that the E_{CB} potential of 1.0 % Pd/H-TiO_2 catalyst was shifted to more negative direction. The elevated energy band structure enhanced the catalyst's

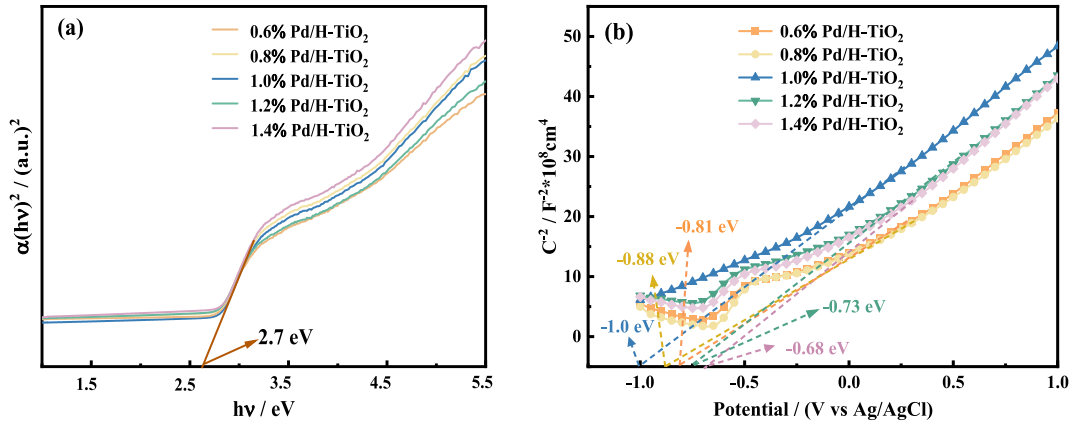

Fig. 6. (a) Tauc plots of x wt%Pd/H-TiO_2 catalysts; (b) Mott-Schotty curves of x wt%Pd/H-TiO_2 catalysts at 2000 Hz.

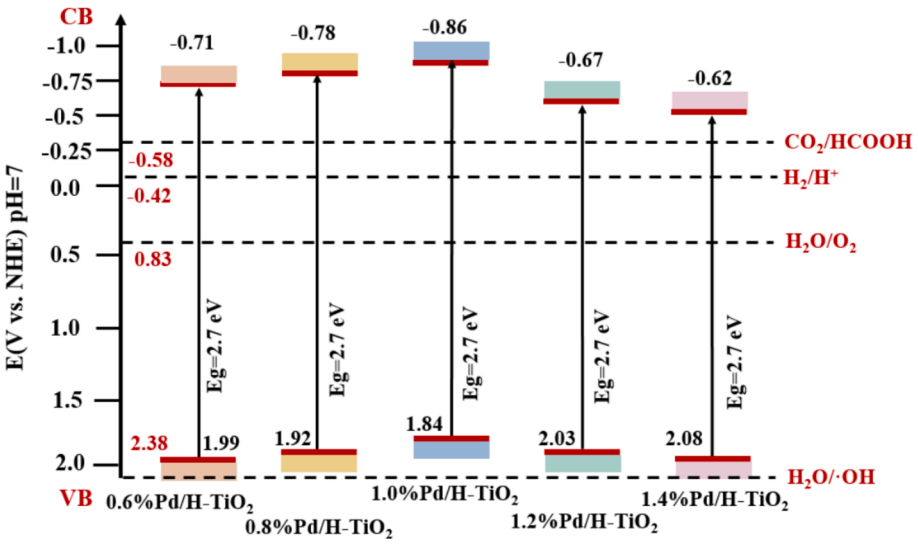

Fig. 7. Energy band structure of a series of x wt% Pd/H-TiO_2 catalysts.

capacity to convert CO_2 to HCOOH, although its oxidizing capability was somewhat diminished (Huang et al., 2022). Therefore, 1.0 % Pd/H-TiO_2 catalyst had the highest photocatalytic activity and the greatest HCOOH production rate.

The electron-hole separation performance of x wt%Pd/H-TiO_2 catalysts by measuring photocurrent response and PL spectroscopy in Fig. 8a-b. The intensity of the photocurrent response of the catalyst exhibited a pattern of initial increase followed by a subsequent decrease as the loading amounts of Pd were increased. The maximum photocurrent response intensity of the 1.0 % Pd catalyst indicates the optimized electron-hole separation performance. This suggests that proper metal loading serves to separate electron-hole pairs and improves charge transfer, which is more conducive to photocatalytic reactions in the liquid phase (Zhu et al., 2020; Ren et al., 2024). Furthermore, the signal intensities of the catalysts in the PL spectra show an opposite trend and the lowest intensity of 1.0 %Pd/H-TiO_2 catalyst demonstrated that it exhibited the smallest recombination rate of electron-hole pairs. The results confirmed that loading of metal Pd effectively enhanced the electron-hole separation and transfer of catalysts within a certain range.

Meanwhile, the carrier concentration of x wt%Pd/H-TiO_2 catalysts via equation (6), which agreed the photocurrent response results (Table S5). The charge density of 1.0 %Pd/H-TiO_2 catalysts ($N_d = 1.76 \times 10^{19}$) was higher than other catalysts, showing that metal Pd doping increases the carrier density. An excessive increase in metal active sites is detrimental to electron-hole separation. As the increase of electron traps leads to easier complexation of electron-hole makes the electron density decrease.

$$N_d = \frac{2/\varepsilon\varepsilon_0 e_0}{d(1/C^2)/dV} \tag{6}$$

where N_d is charge density of catalyst, ε is dielectric constant, ε_0 is vacuum dielectric constant, e_0 is electrical charge, $d(1/C^2)/dV$ is slope of the M−S curve.

Fig. 9 shows the influencing factors of HCOOH production rate and the adsorption conversion steps of CO_2. The findings indicate that the adsorption properties and charge density of CO_2 are enhanced by increasing the electron density at the active site. The increase in reactant concentration and charge concentration were the key factors for the increase in HCOOH production rate.

4. Conclusions

This study demonstrates that rational electron density engineering of Pd active sites via impregnation-hydrogenation synthesis can simultaneously address the critical bottlenecks of CO_2 adsorption and charge carrier separation in TiO_2-based photocatalysis. By precisely modulating Pd loading (0.6–1.4 wt%), the optimal 1.0 wt%Pd/H-TiO_2 catalyst

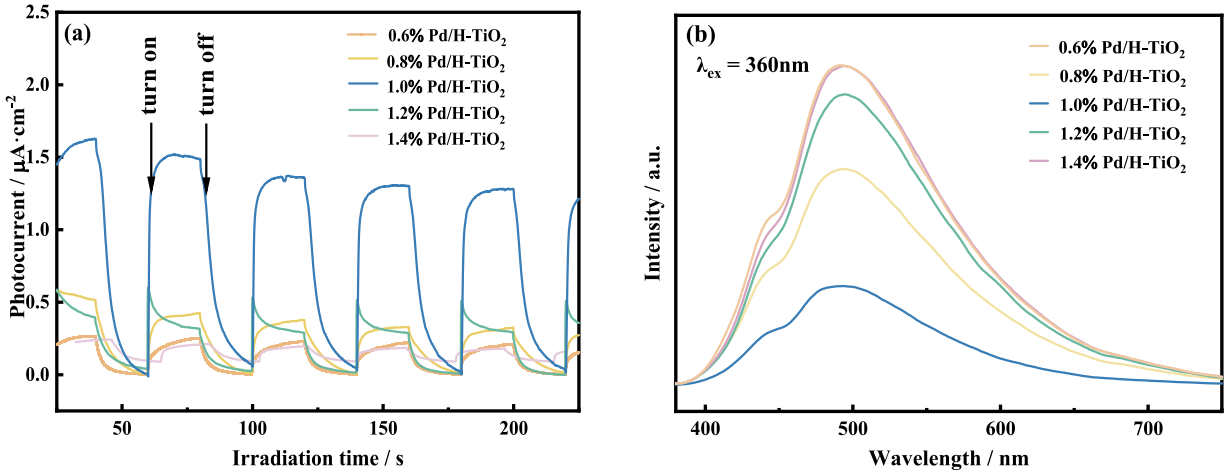

Fig. 8. (a) Photocurrent response; (b) Steady-state PL spectra of x wt%Pd/H-TiO_2 catalysts under 360 nm excitation.

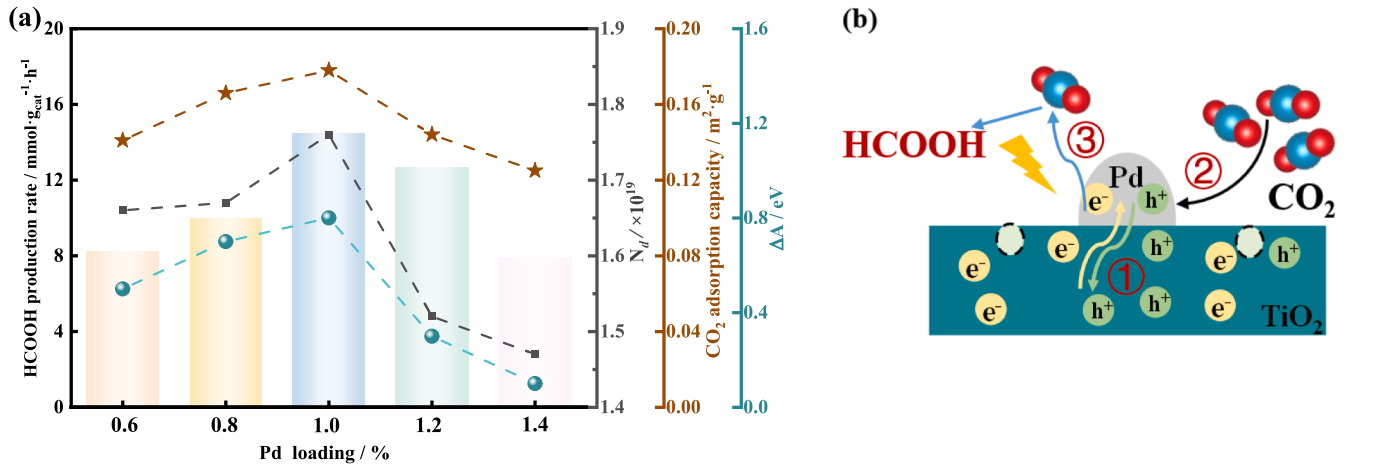

Fig. 9. (a) HCOOH production rate on x wt%Pd/H-TiO_2 as a function of CO_2 adsorption, carrier concentration and electron density of the Pd active sites; (b) CO_2 adsorption conversion mechanism.

achieves a HCOOH production rate of 14.14 mmol·g_{cat}^{-1}·h^{-1} with 1.43-fold enhancement over pristine H-TiO_2, alongside a maximized CO_2 adsorption capacity of 0.178 mmol·g^{-1} under 30 °C, 2.0 MPa. DFT-based mechanistic studies demonstrate that Pd serves as electron reservoirs, exhibiting a correlation with the enhanced CO_2 adsorption energy of −0.732 eV. These methods of modulating the electron density of the Pd active sites offer guidance on developing efficient photocatalysts.

CRediT authorship contribution statement

Ruijie Ma: Writing – original draft, Investigation, Data curation. **Huimin Gao:** Writing – original draft, Investigation. **Jinpeng Zhang:** Investigation. **Jieying Jing:** Writing – review & editing, Supervision, Funding acquisition. **Wen-Ying Li:** Writing – review & editing, Funding acquisition.

Declaration of competing interest

The authors declare that they have no known competing financial interests or personal relationships that could have appeared to influence the work reported in this paper.

Acknowledgments

This work was financially supported by National Key Research and Development Program of China (2022YFE0208400), Natural Science Foundation of Shanxi Province (202303021221019), the Fundamental Research Funds for the Central Universities (2022ZFJH004).

Appendix A. Supplementary data

Supplementary data to this article can be found online at https://doi.org/10.1016/j.ces.2025.122485.

Data availability

Data will be made available on request.

References

Wang, S.W., Wang, L.G., Wang, D.S., et al., 2023. Recent advances of single-atom catalysts in CO_2 conversion. Energ. Environ. Sci. 16 (7), 2759–2803. https://doi.org/10.1039/d3ee00037k.

Xu, R., Si, D.-H., Zhao, S.-S., et al., 2023. Tandem photocatalysis of CO_2 to C_2H_4 via a synergistic rhenium-(I) bipyridine/copper-porphyrinic triazine framework. J. Am. Chem. Soc. 145 (14), 8261–8270. https://doi.org/10.1021/jacs.3c02370.

Rumayor, M., Dominguez-Ramos, A., Irabien, A., 2018. Formic acid Manufacture: carbon dioxide utilization alternatives. Appl. Sci.-Basel 8 (6), 914. https://doi.org/10.3390/app8060914.

Bi, Q.Y., Lin, J.D., Liu, Y.M., et al., 2016. Dehydrogenation of formic acid at room temperature: boosting palladium nanoparticle efficiency by coupling with pyridinic-nitrogen-doped carbon. Angew. Chem.-Int. Ed. 55 (39), 11849–11853. https://doi.org/10.1002/anie.201605961.

Zhao, J.J., Wang, J.Q., Bai, Y., et al., 2023. Mesoporous Ru(Co, Ni)B bimetallic amorphous alloy for CO_2 hydrogenation to formic acid. J. CO2 Util. 74, 102528. https://doi.org/10.1016/j.jcou.2023.102528.

Wagner, A., Sahm, C.D., Reisner, E., 2020. Towards molecular understanding of local chemical environment effects in electro- and photocatalytic CO_2 reduction. Nat. Catal. 3 (10), 775–786. https://doi.org/10.1038/s41929-020-00512-x.

Wang, H.N., Zou, Y.H., Sun, H.X., et al., 2021. Recent progress and perspectives in heterogeneous photocatalytic CO_2 reduction through a solid-gas mode. Coord. Chem. Rev. 438, 213906. https://doi.org/10.1016/j.ccr.2021.213906.

Ma, J., Li, L., Zhang, Y., et al., 2024. Covalent organic frameworks: synthesis, structures, characterizations and progress of photocatalytic reduction of CO_2. Chin. J. Struct. Chem. 43 (12), 100466. https://doi.org/10.1016/j.cjsc.2024.100466.

Alamgir, Mushtaq, M., Ahmad, A., et al., 2025. Shaping the future of solar-driven photocatalysis by reticular framework materials. J. Mater. Sci. Technol. 231, 193–244. https://doi.org/10.1016/j.jmst.2025.02.009.

Habisreutinger, S.N., Schmidt-Mende, L., Stolarczyk, J.K., 2013. Photocatalytic reduction of CO_2 on TiO_2 and other semiconductors. Angew. Chem.-Int. Ed. 52 (29), 7372–7408. https://doi.org/10.1002/anie.201207199.

Pan, H.Q., Heagy, M.D., 2020. Photons to formate: a review on photocatalytic reduction of CO_2 to formic acid. Nanomaterials 10 (12), 2422. https://doi.org/10.3390/nano10122422.

Zhang, S.Q., Yu, H.Y., Wang, Y., et al., 2023. Surface dual metal occupations in Fe-doped $FeBi_2O_3$ induce highly efficient photocatalytic CO_2 reduction. ACS Appl. Mater. Interfaces 15 (20), 25049–25057. https://doi.org/10.1021/acsami.3c02784.

He, H., Ren, Y., Zhu, Y.-H., et al., 2025. Continuous flow photothermal catalytic CO_2 reduction: materials, mechanisms, and system design. ACS Catal. 15 (12), 10480–10520. https://doi.org/10.1021/acscatal.5c02269.

Xiong, J., Yang, A.J., Sun, Q., et al., 2023. Insights into CO_2 activation and charge transfer in photocatalytic reduction of CO_2 on pure and metal single atom modified TiO_2 surfaces. Mol. Catal. 547, 113370. https://doi.org/10.1016/j.mcat.2023.113370.

Cao, Y.H., Guo, R., Ma, M.Z., et al., 2024. Effects of electron density variation of active sites in CO_2 activation and photoreduction: a review. Acta Phys. Chim. Sin. 40 (1), 2303029. https://doi.org/10.3866/pku.Whxb202303029.

Xiong, Z., Wang, H.B., Xu, N.Y., et al., 2015. Photocatalytic reduction of CO_2 on Pt^{2+}-Pt^0/TiO_2 nanoparticles under UV/Vis light irradiation: a combination of Pt^{2+} doping and Pt nanoparticles deposition. Int. J. Hydrogen Energy 40 (32), 10049–10062. https://doi.org/10.1016/j.ijhydene.2015.06.075.

Cao, Y.H., Guo, L., Dan, M., et al., 2021. Modulating electron density of vacancy site by single Au atom for effective CO_2 photoreduction. Nat. Commun. 12 (1), 1675. https://doi.org/10.1038/s41467-021-21925-7.

Ma, M.Z., Huang, Z., Li, L.A., et al., 2023. Modulating photogenerated electron density of Pr single-atom sites by coordination environment engineering for boosting photoreduction of CO_2 to CH_3OH. Appl. Catal. B-Environ. Energy 330, 122626. https://doi.org/10.1016/j.apcatb.2023.122626.

Jin, B.B., Ye, X., Zhong, H., et al., 2020. Light-Driven hydrogenation of bicarbonate into formate over nano-Pd/TiO_2. ACS Sustain. Chem. Eng. 8 (17), 6798–6805. https://doi.org/10.1021/acssuschemeng.0c01616.

Zheng, M.Y., Yang, J., Fan, W.L., et al., 2021. Oxygen vacancy and nitrogen doping collaboratively boost performance and stability of TiO_2-supported Pd catalysts for

CO_2 photoreduction: a DFT study. PCCP 23 (43), 24801–24813. https://doi.org/10.1039/d1cp03693a.

Li, J., Zhou, H., Zhuo, H., et al., 2018. Oxygen vacancies on TiO_2 promoted the activity and stability of supported Pd nanoparticles for the oxygen reduction reaction. J. Mater. Chem. A 6 (5), 2264–2272. https://doi.org/10.1039/c7ta09831f.

Permporn, D., Khunphonoi, R., Wilamat, J., et al., 2022. Insight into the roles of metal loading on CO_2 photocatalytic reduction behaviors of TiO_2. Nanomaterials 12 (3), 474. https://doi.org/10.3390/nano12030474.

Wang, D., Liu, Z.P., Yang, W.M., 2018. Revealing the size effect of platinum cocatalyst for photocatalytic hydrogen evolution on TiO_2 support: a DFT study. ACS Catal. 8 (8), 7270–7278. https://doi.org/10.1021/acscatal.8b01886.

Schweinberger, F.F., Berr, M.J., Döblinger, M., et al., 2013. Cluster size effects in the photocatalytic hydrogen evolution reaction. J. Am. Chem. Soc. 135 (36), 13262–13265. https://doi.org/10.1021/ja406070q.

Zhang, Z.Y., Wang, Z., Cao, S.W., et al., 2013. Au/Pt nanoparticle-decorated TiO_2 nanofibers with plasmon-enhanced photocatalytic activities for solar-to-fuel conversion. J. Phys. Chem. C 117 (49), 25939–25947. https://doi.org/10.1021/jp409311x.

Sun, M.Z., Huang, B.L., 2022. Neighboring effects of active sites for CO_2 transition to C1 products on atomic catalysts. Nano Energy 99, 107398. https://doi.org/10.1016/j.nanoen.2022.107398.

Etim, U.J., Zhang, C.C., Zhong, Z.Y., 2021. Impacts of the catalyst structures on CO_2 activation on catalyst surfaces. Nanomaterials 11 (12), 3265. https://doi.org/10.3390/nano11123265.

Gao, W., Chi, H.Q., Xiong, Y.J., et al., 2023. Comprehensive Insight into construction of active sites toward steering photocatalytic CO_2 conversion. Adv. Funct. Mater., 2312056 https://doi.org/10.1002/adfm.202312056.

Zhang, H.B., Wang, Y., Zuo, S.W., et al., 2021. Isolated cobalt centers on $W_{18}O_{49}$ nanowires perform as a reaction switch for efficient CO_2 photoreduction. J. Am. Chem. Soc. 143 (5), 2173–2177. https://doi.org/10.1021/jacs.0c08409.

Iguchi, S., Kikkawa, S., Teramura, K., et al., 2016. Investigation of the electrochemical and photoelectrochemical properties of Ni-Al LDH photocatalysts. PCCP 18 (20), 13811–13819. https://doi.org/10.1039/c6cp01646d.

Huang, X.Y., Lei, R., Yuan, J., et al., 2021. Insight into the piezo-photo coupling effect of $PbTiO_3$/CdS composites for piezo-photocatalytic hydrogen production. Appl. Catal. B-Environ. 282, 119586. https://doi.org/10.1016/j.apcatb.2020.119586.

Huang, M., Zhang, S.Y., Wu, B., et al., 2022. Selective photocatalytic oxidation of methane to oxygenates over Cu-W-TiO_2 with significant carrier traps. ACS Catal. 12 (15), 9515–9525. https://doi.org/10.1021/acscatal.2c02424.

Zhu, S., Chen, X.F., Li, Z.C., et al., 2020. Cooperation between inside and outside of TiO_2: Lattice Cu^+ accelerates carrier migration to the surface of metal copper for photocatalytic CO_2 reduction. Appl. Catal. B-Environ. 264, 118515. https://doi.org/10.1016/j.apcatb.2019.118515.

Ren, Y., Si, Y., Du, M., et al. Photothermal Synergistic Effect Induces Bimetallic Cooperation to Modulate Product Selectivity of CO_2 Reduction on Different CeO_2 Crystal Facets[J], 2024, 63(46): e202410474. https://doi.org/https://doi.org/10.1002/anie.202410474.